Building deformation caused by tunneling: centrifuge modeling

Article *in* Journal of Geotechnical and Geoenvironmental Engineering · March 2020

DOI: 10.1061/%28ASCE%29GT.1943-5606.0002223

4 authors:

Stefan Ritter
Norwegian Geotechnical Institute

Giorgia Giardina
University of Bath

Andrea Franza
Universidad Politécnica de Madrid

Matthew J. DeJong
University of California, Berkeley

BUILDING DEFORMATION CAUSED BY TUNNELLING: CENTRIFUGE MODELLING

Stefan Ritter[1], Giorgia Giardina[2], Andrea Franza[3], and Matthew J. DeJong[4]

[1]Project advisor I, Onshore Foundations, Norwegian Geotechnical Institute, Sognsveien 72, 0855 Oslo, Norway, Email: stefan.ritter@ngi.no

[2]Assistant Professor, Department of Architecture and Civil Engineering, University of Bath, Claverton Down, Bath BA2 7AY, UK: G.Giardina@bath.ac.uk

[3]Research fellow, ETSI Caminos, Universidad Politécnica de Madrid, Calle del Prof. Aranguren 3, 28040 Madrid, Spain, Email: andreafranza@gmail.com

[4]Assistant Professor, Department of Civil and Environmental Engineering, University of California, 760 Davis Hall, Berkeley, CA 94720-1710, USA, Email: dejong@berkeley.edu

ABSTRACT

This paper investigates the deformation of buildings due to tunnelling-induced soil displacements. Centrifuge model tests of three-dimensionally (3D) printed building models subject to a plane-strain tunnel excavation in dense, dry sand are discussed. The small-scale structures replicate important building characteristics including brittle material properties similar to masonry, a realistic building layout, façade openings, strip footings and a rough soil-structure interface. Digital images were captured during the experiments, enabling image-based measurements of the building response. Results demonstrate the essential role of the building-to-tunnel position and structural details (i.e. opening percentage and building length). The onset of building cracking and cracking patterns confirms the importance of the building-to-tunnel position and structural details. The tests illustrate that an increase in the façade opening area leads to increased shear deformations while longer buildings caused an increase in bending deflections. An evaluation of the widely accepted

framework of treating a structure separately at either side of the greenfield inflection point shows that this procedure can underestimate building damage.

INTRODUCTION

Underground construction involves ground movements, which threaten the urban fabric. To accurately assess the risk of building damage during tunnelling requires an adequate description of the soil–structure interaction. Several procedures (e.g. Potts and Addenbrooke (1997); Franzius et al. (2006); Son and Cording (2005); Goh and Mair (2011b); Franza et al. (2017)) have been proposed to account for this interaction; however, limitations and inconsistencies about their accuracy and reliability exist (Giardina et al., 2018; DeJong et al., 2019). Particularly, the effect of structural details (e.g. building position, façade openings and building dimensions) on this complex interaction problem requires further research.

While extensive case studies (e.g. Burland et al. (2004); Mair (2013); Standing (2001); Viggiani and Standing (2001); Dimmock and Mair (2008); Bilotta et al. (2017)) revealed important trends, field data is inherently affected by various assumptions related to the tunnel excavation, the ground conditions and the asset. Previous computational (Potts and Addenbrooke, 1997; Franzius et al., 2006; Goh and Mair, 2011c) and experimental (Al Heib et al., 2013; Caporaletti et al., 2005; Taylor and Grant, 1998; Taylor and Yip, 2001; Farrell, 2010) studies mainly focused on the impact of the overall building stiffness and thus replicated buildings as simple plate or beam models. Specifically, existing centrifuge model tests, which accurately replicate the self-weight stress state in both the structure and the soil, were limited to simple small-scale building models in the form of rubber, aluminium, micro-concrete and masonry plates or beams (Caporaletti et al., 2005; Farrell and Mair, 2010; Taylor and Grant, 1998; Taylor and Yip, 2001). However, more recent computational modelling research showed the essential role of building features including stress localisation effects in the vicinity of wall openings (Burd et al., 2000; Giardina et al., 2013; Son and Cording, 2007; Pickhaver et al., 2010; Yiu et al., 2017) and the non-linear behaviour of the building material (Amorosi et al., 2014; Giardina et al., 2015; Boonpichetvong and Rots, 2005; Son and Cording, 2007; Yiu et al., 2017). Consequently, there is a lack of experimental data about the impact of building details on this tunnel–soil–structure interaction system.

Uncertainty still exists regarding the governing mode of building deformation (i.e. shear (Son and Cording, 2005, 2007) or bending (Potts and Addenbrooke, 1997; Franzius et al., 2006; Goh and Mair, 2011c)) due to tunnelling. Widely accepted frameworks of estimating potential damage of buildings adjacent to tunnel excavation focus only on the assumed critical mode of building deformation and thus treat the relative importance of shear or bending distortions differently. Assuming a governing deformation behaviour results in the specification of different building deformation parameters related to bending or shear deformations, which is evident in the formulations of the different relative stiffness methods (Son and Cording, 2005; Potts and Addenbrooke, 1997; Franzius et al., 2006; Goh and Mair, 2011c). Moreover, there has been little agreement on the ratio of the bending to the shear stiffness, E/G, and the aspect ratios, L/H, which determine the predominance of bending or shear deformations (Burland and Wroth, 1974; Cook, 1994; Devriendt, 2003; Mair et al., 1996; Melis and Rodriguez Ortiz, 2001; Son and Cording, 2007). In particular, experimental data on the effect of building features on the critical mode of building distortions is still missing.

Existing methods to estimate the potential risk of building damage caused by tunnelling often partition a building at the greenfield inflection point and separately assess either part (Mair et al., 1996; Goh and Mair, 2011a). However, the soil–structure interaction modifies the length of the theoretical greenfield displacement modes (i.e. sagging and hogging) as identified by Farrell (2010); Frischmann et al. (1994); Lu et al. (2001); Potts and Addenbrooke (1997); Franza et al. (2018). This implies that treating a building separately either side of the greenfield inflection point might underestimate the degree of structural damage (Netzel, 2009).

The aim of this paper is to provide experimental data of more realistic building models subjected to tunnelling-induced soil displacements to understand the vital role of building features on the building displacements. More specifically, the influence of building details (e.g. building-to-tunnel position, façade opening area, length) on building deformations are revealed at global and local scale, building cracking damage is discussed, the effect of building features on the predominant role of shear or bending distortions is quantified and the widely applied partitioning approach is evaluated.

CENTRIFUGE MODELLING PROCEDURE

Fig. 1 introduces the performed centrifuge tests, which were conducted at 75 times the Earth's gravity field. A shallow tunnelling scenario with a cover-to-diameter ratio, C/D_t, of 1.35 was modelled and a plane-strain tunnel excavation in dry, dense sand was conceptually replicated by reducing the tunnel volume. This technique enabled simulation of various tunnel volume loss values, $V_{l,t}$, in a single experiment. The ground conditions were kept constant for each test in the test series by pouring Leighton Buzzard Fraction E silica sand to a relative soil density, I_D, of 90% (±3%), but different building lengths, different building positions relative to the tunnel and different opening areas were studied (Fig. 1 and Table 1).

Powder-based 3D printing was employed to create representative small-scale structural models with building details such as façade openings, strip footings, a rough soil-structure interface and intermediate walls at 1/75th of prototype scale. These model buildings were placed on the soil with their long direction perpendicular to the tunnel. Fig. 2 shows that the building models consisted of front, rear and end walls, which were supported by strip footings, and two or three partitioning walls depending on the building length. A constant bearing pressure of 100 kPa beneath the front and rear strip footings was replicated by adding dead load bars on the top of the building models. For the entire footprint an average bearing pressure of 80 kPa was calculated. An average bearing pressure of 80 kPa was calculated through dividing the total building load, including self-weight as well as the dead load bars, with the soil-structure contact area. The 3D printed material exhibits brittle behaviour similar to masonry and overall axial stiffness, EA, and bending stiffness, EI, values in the range of reported field data (Table 1). The EA and EI values of the building models were obtained by adopting the frameworks outlined by Pickhaver et al. (2010) and Melis and Rodriguez Ortiz (2001), respectively. These approaches account for a stiffness reduction due to façade openings, which is often neglected in historical field data (e.g. Mair and Taylor (1997)). In addition, a stiffness reduction due to geometrical differences in the direction parallel to the tunnel was considered by reducing the stiffness of the façades and foundation to per meter values following

Farrell (2010). The second moment of area of a cross-section of the building, I, was estimated with respect to an average neutral axis of the cross-section, considering walls, openings and foundations (Table 1). To measure building and soil displacements, an image-based measurement technique, GeoPIV (White et al., 2003), was adopted. A detailed description of the experimental techniques is reported elsewhere (Ritter et al., 2017b; Ritter, 2017; Ritter et al., 2018).

PROCESSING EXPERIMENTAL DATA

Son and Cording (2005) subdivided a building adjacent to a deep excavation into building units (or bays) based on the location of intermediate walls, building columns, different structural properties (e.g. geometry or stiffness) or gradients of ground displacements. Fig. 3 shows such a building unit, including the four corner points of the building unit and schematic building deformation. Based on horizontal, S_h, and vertical displacements, S_v, of the corner points, the building height, H, and the length of the building unit, L_u, the response of the buildings to the tunnelling-induced settlements was quantified. Fig. 3 and the following equations define the building deformation parameters, originally reported by Son and Cording (2005):

Base horizontal strain:

$$\varepsilon_{h,base} = \frac{S_{h,B} - S_{h,A}}{L_u} \tag{1}$$

Top horizontal strain:

$$\varepsilon_{h,top} = \frac{S_{h,C} - S_{h,D}}{L_u} \tag{2}$$

Slope:

$$s = \frac{S_{v,A} - S_{v,B}}{L_u} \tag{3}$$

Tilt (rigid body rotation):

$$\theta = \frac{(S_{h,A} - S_{h,D}) + (S_{h,B} - S_{h,C})}{2H} \tag{4}$$

Angular distortion:

$$\beta = s - \theta = s - \frac{\omega_1 + \omega_2}{2} \tag{5}$$

The adopted tilt definition (Equation 4), eliminates bending contributions when computing the angular distortion (Equation 5). From Equations 4 and 5, it can be followed that $\omega_1 = \frac{S_{h,A} - S_{h,D}}{H}$ and $\omega_2 = \frac{S_{h,B} - S_{h,C}}{H}$.

Fig. 3 shows that the building deformation parameters are a result of the displacements of the points A, B, C and D, which can be either the corner points of the entire structure or a certain unit of the building. Global behaviour of a building was estimated by using the displacements of the corner points of the entire structure, whereas the local behaviour was evaluated by subdividing the building into bays or half-bays (i.e. distance between pier centrelines on either side of a single window). Fig. 4 depicts the building subdivision into bays for a building configuration with L = 260 mm, where $L_u \approx L/4$, and the notation of corner points. For buildings with L = 200 mm, only three building bays with the corner points 1-8 exist.

To distinguish between bending and shear displacements (and deformations), the framework outlined by Cook (1994) was adopted. Fig. 5 defines the sign convention and tilt and bending deformations. For each bay or half-bay the following steps were carried out:

Firstly, the displacement due to tilt was defined as:

$$S_{v,tilt} = \omega_2 L_u \,. \tag{6}$$

where ω_2 is in radians. Secondly, the bending displacement was derived as

$$S_{v,bend} = \chi \frac{L_u^2}{2} = \Delta\omega \frac{L_u}{2} \tag{7}$$

where χ is the average curvature, $\Delta\omega = \omega_1 - \omega_2$ and positive values of $S_{v,bend}$ indicate a hogging (i.e. convex) mode of deflection. Thirdly, the total vertical displacement was computed as:

$$S_{v,tot} = S_{v,A} - S_{v,B} \,. \tag{8}$$

Finally, the shear displacement was defined as:

$$S_{v,shear} = S_{v,tot} - S_{v,tilt} - S_{v,bend} \tag{9}$$

and the shear strains of a building unit can be directly estimated from $S_{v,shear}$:

$$\gamma = \frac{S_{v,shear}}{L_u} = s - \frac{\omega_1 + \omega_2}{2}. \tag{10}$$

Note that γ and β (Equation 5) are equal.

The above procedure assumes constant curvature over a single building unit when estimating bending displacements. Likewise, uniform shear deflection is assumed, and the shear displacements are defined as the displacements that are not related to the tilt or bending components (Equation 9). This framework depends on the used length of the building unit. Reducing the building unit length (e.g. from bay to half-bay) reduces the errors due to assumptions of constant bending and shear over a single building bay.

The Cook (1994) method can be used to approximately estimate average bay curvature and shear strain from bay corner displacements. Its efficiency was evaluated analytically with respect to the displacement data of a simply supported Timoshenko beam subjected to a concentrated load. Averaged shear strain and curvature of the bay were in satisfactory agreement with the exact solution when partitioning the structures into bays or half-bays.

RESULTS

First, the global building response (using the four corner points at the building corners) is analysed. Second, the local building response is illustrated by subdividing the buildings into bays at the position of the partitioning walls (Fig. 4). Third, a mechanical interpretation using half-bay subdivisions is performed, after which building damage is discussed.

Global building response

The global building response is estimated by using the entire extent of the building as building unit. Fig. 6 presents the building deformation parameters of the entire test series. As expected, compressive or tensile top horizontal strains were measured for a building predominantly placed in the greenfield sagging (test A) or hogging region (test B), respectively. Surprisingly, test C, which spans the greenfield inflection point, showed substantial top compressive strains; tensile strains would be expected if hogging was dominating the response. For test D, tensile top horizontal strains were derived, similar to test B. Long structures (tests E and F) placed in the hogging/sagging transition region of the respective greenfield settlement profile showed considerable tensile strains at the top. The greatest tensile strain was observed for test F which implies that a long structure with a significant amount of window openings (i.e. 40%) placed in the greenfield hogging and sagging region is likely to be exposed to a significant risk of building damage. The increase in $\varepsilon_{h,top}$ for test F after $V_{l,t}$ = 2.5% can be related to building damage and global softening (Section 4).

For all tests, the magnitude of base horizontal strains (Fig. 6b) were significantly lower than the top horizontal strains. This is likely to be caused by the rough soil–structure interface; friction between the soil and the underside of structure limits the horizontal strains at the base of the structure. Similar observations have been made from field data (e.g. Standing (2001); Burland et al. (2004)) and physical model test data (Farrell and Mair, 2010). This mechanism likely moves the position of zero strain from the neutral axis of the building cross-section (Table 1) to a position closer to the foundation level, which explains the increase in top horizontal strains. For the tests with buildings located in the hogging zone (tests B and D) tensile base strains were obtained. This indicates that the strain induced by horizontal soil displacements dominated over the base horizontal strain caused by hogging (bending) deformations. For structures placed in the greenfield hogging/sagging transition zone, the window opening percentage caused a considerable difference in the response. Buildings with 20% of openings (tests C and E) were in compression at the base while the tests D and F were in tension. It is likely that the structures with 20% openings responded primarily in bending while the structures with 40% of openings showed mainly shear deformations;

this aspect will be further considered in Section 5. Additionally, the increase in opening area caused a reduction in the axial building stiffness, EA, which increased the axial flexibility of the structures in the tests D and F.

Fig. 6c indicates that the slope and tilt values are a function of the eccentricity. Notably, the buildings with one edge directly above the tunnel (tests C, E, and F) experienced the greatest global slope, followed by the buildings in the hogging region (tests B and D), whereas negligible slope values were measured for test A as was expected.

Similar trends are also evident for the tilt (Fig. 6d). In all tests, the global tilt and slope values are nearly identical which results in relatively low values for the global angular distortion (Fig. 6). This observation is a result of the adopted tilt definition (Equation 4) that averages the tilt measured at the left and right building end walls and suggests small structural deformations. The high global slope and tilt values observed in tests C, E and F can be related to rigid body rotation and, thus, are less important for damage predictions, but can cause serviceability problems.

Fig. 6e presents the angular distortion against $V_{l,t}$. This global angular distortion is indicative of the average shearing distortion of the building, assuming that the strain is constant over the entire building length. This assumption is a considerable simplification; a detailed evaluation of more local deformations follows below. However, the global angular distortion still gives a measure of structural deformations and is indicative of potential building damage. The global measure of angular distortion indicates a significant potential for cracking of the buildings spanning the greenfield inflection point (tests C, E and F), while negligible angular distortion values were observed for the tests A, B and D. Particularly when taking the notable tensile strains measured at the top of tests E and F into account, the location, increased length and percentage of façade openings tend to result in substantial susceptibility to building damage.

Local building response

Localisation effects of building damage are discussed next for each bay, by subdividing the buildings at their intermediate walls (Fig. 4). For every building bay, the displacements of the corner points are estimated, and subsequently the deformation parameters derived. Figs. 7, 8 and

9 compare the top horizontal strain, base horizontal strain and the angular distortion, respectively. These building deformation parameters, which are related to bending and shear distortions, are of key importance when assessing potential building damage. However, again, these parameters assume constant deformation over the length of a building bay and thus do not directly quantify bending or shear deformations. In addition, parts of the horizontal strain are caused by axial deformations, which cannot be decoupled from bending.

When the structure was placed in the sagging region of the settlement trough (test A), compressive horizontal strains occurred in all building bays, as is evident from Figs. 7a and 8a. By contrast, the angular distortion of Bay 2 remained close to zero, while a similar magnitude of angular distortion but with different sign was measured for Bay 1 and 3 (Fig. 9a). These results for the angular distortion were to be expected due to the symmetric position of the building model in test A, for which the maximum shear would occur at approximately the quarter points in the structure (see Section 4).

Figs. 7b, 8b and 9b summarise the $\varepsilon_{h,top}$, $\varepsilon_{h,base}$ and β values for the different bays of test B. For the structure placed in the hogging region, top tensile strains were measured throughout all bays (Fig. 7b). The greatest $\varepsilon_{h,top}$ was measured in Bay 2, and indicates potential tension cracking in this region which is in agreement with the observed building damage, as discussed below. Similarly, the greatest $\varepsilon_{h,base}$ was determined in Bay 2 (Fig. 8b), but notably smaller than $\varepsilon_{h,top}$. For Bay 1, minor compressive $\varepsilon_{h,base}$ were observed. These measurements indicate that hogging occurred across all bays, but was largest in Bay 2, as expected. The angular distortion estimated for Bay 2 was close to zero while considerable angular distortion values were calculated for the Bays 1 and 3, again of opposite orientation as expected (Fig. 9b). The considerable amount of angular distortion in Bays 1 and 3 suggests shear deformation, which would again be expected to be maximum at approximately the quarter points. This indicates that beam theory approaches may be applicable for this building-to-tunnel position.

The building model of test C experienced substantial compressive strains in Bay 1 (Figs. 7c and 8c) whereas top horizontal tensile strains were observed in Bay 2 (Fig. 7c). In Bay 3 the top horizontal strains remained close to zero for the tunnel volume losses considered. The significant compressive strain observed in Bay 1 is likely due to the embedment of the left building corner into the soil, restraining the horizontal displacement at the left bottom building corner, combined with the substantial rigid body rotation towards the tunnel and horizontal movements shifting the building towards the tunnel centreline. Similarly to test B, the angular distortion for Bay 1 and Bay 3 were of opposite sign, but in this case Bay 1 shows larger values, while the angular distortion calculated for Bay 2 was close to zero. This suggests that the global response of test C is primarily hogging, which would indicate that the left corner embedment primarily provides a horizontal reaction, but not a vertical reaction large enough to significantly change the bending behaviour.

Figs. 7d and 8d show that minor horizontal building strains were transferred to the structure of test D. A comparison with test B (Figs. 7b and 8b) indicates that an increase in the window openings from 20% to 40% for test D but identical building-to-tunnel position and length had a minor impact on the horizontal building strains. By contrast, the angular distortions of Bays 1 and 3 of test D, shown in Fig. 9d, nearly doubled compared to test B (Fig. 9b). This rise in β can be attributed to the increased shear flexibility due to the greater opening percentage. This is in agreement with strip method calculations (Ritter, 2017) that estimate a decrease of 21% in the facade shear stiffness.

For the long buildings placed at $L/H = 0.5$ (tests E and F), the greatest horizontal top tensile strains were measured in Bays 2 and 3 (Figs. 7e and f). By contrast, $\varepsilon_{h,top}$ is almost negligible in Bays 1 and 4. This is again indicative that these buildings are behaving primarily in hogging; any potential embedment effect at the left corner is only evident in Bay 1 of test F, in which compressive strains are again observed, similar to test C. Note that to keep a constant scale for the entire test series, the horizontal top tensile strains for Bay 2 of test F are not shown after reaching 0.125%. The substantial rise of these tensile strain is related to building cracking. Fig. 8e shows that notable horizontal strains were transferred to the base of the Bays 1 and 2 of test E. This suggests that test E was primarily in hogging. For test F, only Bay 1 showed compressive strains (Fig. 8f) indicating that the increased opening area reduced the bending contribution to horizontal strains.

A significant amount of angular distortion was measured in Bays 1, 2 and 4 of the tests E and F, as shown in Figs. 9e and f. Tests E and F show very similar behaviour, and again are indicative of a building behaving primarily in hogging. In general, increasing the façade opening percentage further increased the angular distortion values before cracking, after which the angular distortion levelled or decreased due to localization of building strains in cracking elsewhere. In combination with the significant amount of horizontal tensile strains experienced in the Bays 2 and 3 of the tests with structures of L = 260 mm, this finding indicates that long structures spanning the greenfield inflection point (tests E and F) were the most vulnerable scenario studied. For these building-to-tunnel configurations building damage will occur at low tunnel volume loss, as will be explored in Section 4.

Mechanical interpretation

Using the same approach as outlined above, an analysis at half-bay spacing was carried out to aid in mechanical interpretation. Fig. 10 shows the shear strain, γ (Equation 10), and top horizontal strain distribution along the building length. A simplified schematic interpretation of the net loading (w) due to the tunnelling-induced distribution of the building load and the evolution of shear (V) and bending moment (M) distributions is also provided in Fig. 11. Note that this schematic is not exact, but provides a useful approximation to interpret results if pure hogging or sagging displacements were occurring. Note also that this simplified interpretation focuses on the vertical component of the tunnelling-induced displacement field and neglects horizontal displacements.

For test A, the tunnelling-settlements cause a load redistribution to the building corners (Fig. 11a-i). As a consequence, shear forces evolve which concentrate approximately at the building quarter points (Fig. 11a-ii). The experimentally obtained shear distribution (test A in Fig. 10a) is in good agreement with this mechanical interpretation. The related bending moment interpretation is depicted in Fig. 11a-iii. Fig. 10b shows the measured top horizontal strains. The concentration of compressive horizontal strains at the building centre is in accordance with the bending moment interpretation.

The buildings in the greenfield hogging region (tests B and D) are subject to a building load redistribution that concentrates close to the building centre (Fig. 11b-i). Fig. 11b-ii and 11b-iii illustrate the related shear and bending moment interpretations. The observed shear and top horizontal strain distributions (Fig. 10) fit the mechanical explanation. As discussed above, increasing the opening area resulted in an increase of the shear strains, while the top horizontal strains reduced slightly (compare tests B and D in Fig. 10). Note that the increase in window openings decreases the shear stiffness of the building more than the bending stiffness.

A mechanical interpretation of the behaviour of the structures spanning the greenfield inflection point is more difficult. Test C responded primarily in hogging (compare tests B and C in Fig. 10). The notable compressive strain close to the left building corner (Fig. 10b) is likely caused by building rotation and embedment of the left buiding corner (as discussed before). The shear and top horizontal strain results of tests E and F indicate that the structures primarily showed hogging type distortions. Doubling the window opening area increased the shear strains, while a minor reduction of the horizontal strains near the building centre was observed (compare tests E and F in Fig. 10). Due to the increased flexibility of test F, the left building corner experienced a sagging response explaining the compressive horizontal strains.

Building damage

The 3D printed structures exhibit brittle behaviour similar to that of masonry, eventually causing cracking during the centrifuge tests. The ultimate strain to failure, ε_{ult}, of the 3D printed material (Table 1) is about an order of magnitude higher compared to brick and mortar structures; thus, cracking damage is expected at relatively high tunnel volume loss. Within this section, the onset and location of these cracks is identified.

Fig. 12 presents the building damage observed for test F. For all structural models that experienced damage, cracking initiated at the top of the buildings. Horizontal displacement profiles at top building level (Fig. 12a) were used to derive the crack onset. Fig. 12a indicates that crack locations can be identified where a sharp gradient of the horizontal displacement profiles is apparent. In addition, a visual inspection of the corresponding images that were acquired during the experiments was conducted (Fig. 12b). The first visible crack for test F (i.e. crack A in Fig. 12b) emerged at a $V_{l,t}$ of approximately 2.6%. As volume loss developed, the crack propagated vertically towards the base of the structure, causing the cracks B and C in Fig. 12b. Finally, crack D developed.

From Fig. 12 it is apparent that the crack location was close to the window corners. This was expected because openings define the weakest cross-sections and result in stress localisation close to the window corners (Giardina et al., 2015). The predominantly vertical direction of the cracks can be related to the weak interlayer bond between the different layers of the 3D printed material, caused by the powder-based 3D printing procedure (Feng et al., 2015; Ritter et al., 2018). As $V_{l,t}$ developed, the initial cracks grew and a rotation of the two main building parts defined by the initial cracks A-C becomes visible (Fig. 12c). This essentially separated the building into two parts that rotated independently. The portion to the left of the crack rotated towards the tunnel while the right portion experienced notably smaller rotation and displacements.

Fig. 13 visualises the observed crack patterns of all tests. For test A, no cracking occurred, though a gap beneath the building developed at a $V_{l,t}$ of approximately 1.4% and became more pronounced as $V_{l,t}$ increased. The remaining tests showed building damage, but a gap between the foundation and the soil was not observed. Similar trends of crack onset at the top of the building models and vertical development of the cracks towards the base of the structures occurred. The exact location of the first crack may be explained by the distribution of shear and horizontal strains shown in Figure 10.

Table 2 summarises the $V_{l,t}$ at the onset of visible cracking. Buildings that spanned both the greenfield hogging and sagging region with notable window openings (i.e. 40%) were more susceptible to cracking damage which agrees with the measured building deformation parameters. For test F, visible cracking occurred at values of surface soil volume loss ($V_{l,s}$) of approximately 2.0%, which is in fair agreement with often applied design values (e.g. Vu et al., 2016). Micro-cracking, which is evident in some of the data but cannot be identified with the naked eye, might have occurred at slightly lower volume loss values.

DISCUSSION OF BUILDING CHARACTERISTIC EFFECTS ON SHEAR AND BENDING DEFORMATIONS

This section considers the relative importance of shear and bending distortions during building response to tunnelling. Specifically, building length and façade opening effects on the governing mode of building deformation are explored.

Building length effects

The effect of different building lengths on the governing mode of building distortions is studied by two scenarios, which are illustrated in Figs. 14a and 14b. Scenario (a) focuses on building configurations with a constant façade opening percentage of 20% and compares Bay 1 of test B with Bay 2 of test E (Fig. 14a) as highlighted with the arrow. Both bays are located at equal position with respect to the tunnel centreline. Following the same principles, scenario (b) compares building configurations with 40% façade openings (tests D and F, Fig. 14b).

Fig. 14c presents the impact of the building dimensions on bending and shear deflections, which were derived by adopting the Cook (1994) framework (Section 3). For different percentage of window opening area (20% and 40%) an increase in the building length from 200 mm to 260 mm caused greater bending deflections while shear deflections were rather similar. This is particularly true as $V_{l,t}$ increases, and the substantial change of bending and shear deflection in test F indicates cracking initiation at a $V_{l,t}$ of approximately 2.6% (Fig. 14c). Although L/H increased only from 2.2 to 2.9, an increase in the building length combined with the position of the building in the greenfield hogging/sagging region led to substantially higher bending deformations.

Building opening effects

To study the effect of different façade opening percentage, two scenarios are chosen. Fig. 15a shows structures B and D both with $L = 200$ mm and placed in the hogging region of the corresponding greenfield settlement profile but with 20% and 40% openings respectively. Likewise, the buildings of the tests E and F are placed at identical building-to-tunnel position and have equal length but differ in opening area (Fig. 15b). These two scenarios are now used to point out the effect of window opening variations on the shear and bending deformation components.

For buildings with identical length and position relative to the tunnelling-induced settlement profile, an increase in window openings from 20% to 40% caused greater shear deflections while the bending components generally remained close to zero. This finding is evident for buildings with $L/H = 2.2$ (Fig. 15c) and $L/H = 2.9$ (Fig. 15d). Only in Bay 2 of the structures with $L = 260$ mm was a considerable bending contribution measured, as can be seen from Fig. 15d-i.

DISCUSSION OF BUILDING RESPONSE FOR HOGGING AND SAGGING SEPARATION

To evaluate current assessment methods that analyse building parts on either side of the greenfield inflection point separately, the building response is quantified for the hogging and sagging part individually. Therefore, for the building subdivision a theoretical $i = 60$ mm is assumed (Fig. 16), which is identical to the measured greenfield inflection point at $V_{l,t} = 1.0\%$. Fig. 16a illustrates this approach, and indicates that assessment predictions for test B and the hogging part of test E (E_{hog}) would theoretically give the same result. Likewise, the prediction of the behaviour of the sagging part of test C (C_{sag}) would be equal to the prediction for the sagging part of test E (E_{sag}). For buildings with 40% of openings, illustrated in Fig. 16b, the hogging parts of test D (D_{hog}) and test F (F_{hog}) should theoretically result in identical building response. While Mair et al. (1996) reported that building parts exceeding $x = 2.5 \cdot i$, where i is the greenfield inflection point, can be neglected, Netzel (2009) showed that this assumption might lead to underestimation of bending strains. Therefore, within this work the entire building length is considered.

Fig. 16c compares the damage parameters for test B and E_{hog} as $V_{l,t}$ developed. The theoretical hogging part of test E experienced a different response than test B. A considerable greater tensile strain was monitored at the top of test E while the base horizontal strain is rather similar for both tests analysed. The additional extent of the building towards the tunnel in test E caused a significant increase in the slope, as can be seen from Fig. 16c. Similarly, the rigid body rotation (i.e. tilt) measured for the hogging part of test E notably increased compared to the one of test B. Although there is scatter in the GeoPIV data, Fig. 16c indicates a greater angular distortion for E_{hog}. These observations show that test E is more vulnerable to potential building damage than test B.

Fig. 16d compares the response of the theoretical hogging part of test F with test D. The trends evident in Fig. 16d for 40% openings match the observations made for the buildings with 20% of openings (Fig. 16c). These results demonstrate that treating the theoretical sagging and hogging part of a building separately, i.e. subdividing the structure at the greenfield inflection point, can lead to underestimation of building damage.

The building deformation parameters for the sagging parts of test C (C_{sag}) and E (E_{sag}) are presented in Fig. 16e. While the compressive top horizontal strain for C_{sag} is notably greater than for E_{sag}, the remaining parameters indicate a similar response for both tests. As a consequence, the additional building length of test E had a minor influence on the building part in the sagging region. This finding suggests that a sagging/hogging subdivision might result in satisfactory predictions for the sagging part of a building, which generally is the less critical part due to predominantly compressive strains, though additional data is needed to confirm this observation.

CONCLUSION

This paper discusses the results of a series of centrifuge model tests focusing on the effect of different building details on the response of buildings to tunnelling-induced movements. A schematic tunnel excavation in dry, dense sand and complex surface structures with brittle material properties were modelled at $1/75^{th}$ of prototype scale. The vital role of different building layouts, different building positions relative to the tunnel and different percentages of façade opening area was investigated. While the modification of typical greenfield displacements due to soil–structure interaction mechanisms was discussed elsewhere (Ritter et al., 2017a), the experimental data was used to obtain insight into the influence of structural details on the building response and to evaluate the widely accepted partitioning approach.

Son and Cording (2005) and Cook (1994) methods were detailed and used to estimate both global and local (building unit) deformations from the displacements of the top and bottom building levels. Interestingly, under the adopted assumptions, angular distortion and shear strains are identical.

Global and local building deformation data revealed that the building response to tunnelling subsidence and related cracking depends on the building-to-tunnel position and structural details. Structures that were placed in the greenfield hogging/sagging transition regions were more vulnerable to building damage than equal buildings located in either sagging or hogging. Increasing the building length and the façade openings resulted in larger horizontal top tensile strains and angular distortion values. Cracking onset and patterns observed for the different building configurations confirmed the building response, resulting from the analysis of building deformation parameters.

Bending and shear deformation components of buildings subject to tunnelling-induced settlements were experimentally obtained. The results have shown the effect of changing building dimensions and façade opening percentage on the bending and shear deformations. An increase in the building length led to an increase in bending deflections while shear deflections remained rather equal. A larger window opening area caused a considerable increase in the shear component but had little effect on bending deformations. These findings indicate the importance of considering both shear and bending deformations when assessing tunnelling-induced settlement damage on structures.

The widely accepted framework of individually assessing building parts on either side of the greenfield inflection point was evaluated. It was shown that the partitioning approach led to reasonable results for sagging parts of structures. However, hogging parts showed a significantly different structural response if the structure extended across the corresponding greenfield inflection point. This finding was obtained for buildings with different window opening percentage. The obtained results suggest that neglecting the sagging part of a building when evaluating the hogging part might lead to underestimation of the building damage.

Finally, the experimental results provide missing benchmark data of realistic building models subject to tunnelling-induced settlements in order to verify computational models and to evaluate currently available design methodologies that account for the soil–structure interaction.

DATA AVAILABILITY

Some or all data, models, or code generated or used during the study are available in a repository online in accordance with funder data retention policies. The associated research data is available at https://doi.org/10.6078/D1267M.

ACKNOWLEDGEMENTS

The authors are grateful to Prof. Lord R. J. Mair for his valuable comments throughout this research and Dr R. P. Farrell for sharing greenfield data. This work was carried out at while the authors were part of the Department of Engineering, University of Cambridge (UK). Special thanks goes to the Schofield Centre technicians for their assistance. Financially support was provided by the Engineering Physical Sciences Research Council (grant EP/KP018221/1) and Crossrail.

REFERENCES

Al Heib, M., Emeriault, F., Caudron, M., Nghiem, L., and Hor, B. (2013). "Large-scale soil-structure physical model (1g)-assessment of structure damages." *Int. Journal of Physical Modelling in Geotechnics*, 13(4), 138–152.

Amorosi, A., Boldini, D., De Felice, G., Malena, M., and Sebastianelli, M. (2014). "Tunnelling-induced deformation and damage on historical masonry structures." *Géotechnique*, 64(2), 118–130.

Bilotta, E., Paolillo, A., Russo, G., and Aversa, S. (2017). "Displacements induced by tunnelling under a historical building." *Tunnelling and Underground Space Technology*, 61, 221–232.

Boonpichetvong, M. and Rots, J. G. (2005). "Settlement damage of masonry buildings in soft-ground tunnelling." *The Structural Engineer*, 83(1), 32–37.

Burd, H. K., Houslby, G. T., Augarde, C. E., and Liu, G. (2000). "Modelling tunnelling-induced settlement of masonry buildings." *Proc. of the Institution of Civil Engineers-Geotechnical Engineering*, 143(1), 17–29.

Burland, J. B., Mair, R. J., and Standing, J. R. (2004). "Ground performance and building response due to tunnelling." *Proc. Int. Conf. on Advances in Geotechnical Engineering (R.J. Jardine, D.M. Potts and K.G. Higgins eds.), London*, 291–342.

Burland, J. B. and Wroth, C. P. (1974). "Settlement of buildings and associated damage - SOA review." *Proc. Conf. Settlement of structures, Cambridge*, 611–654.

Caporaletti, P., Burghignoli, A., and Taylor, R. N. (2005). "Centrifuge study of tunnel movements and their interaction with structures." *Geotechnical Aspects of Underground Construction in Soft Ground (K.J. Bakker, A. Bezuijen, W. Broere and E.A. Kwast eds.), Amsterdam, The Netherlands, 15-17 June*, 99–105.

Cook, D. (1994). "Studies of settlements and crack damage in old and new facades." *Proc. 3rd Int. Masonry Conf., London, England*, Vol. 6, 203–211.

DeJong, M. J., Giardina, G., Chalmers, B., Lazarus, D., Ashworth, D., and Mair, R. J. (2019). "The impact of the crossrail tunnelling project on masonry buildings with shallow foundations." *Proceedings of the Institution of Civil Engineers - Geotechnical Engineering*, 0(0), 1–35.

Devriendt, M. D. (2003). "Assessing building response at King's X." *Tunnels & Tunnelling International*, 35(7), 24–27.

Dimmock, P. S. (2003). "Tunnelling-induced ground and building movement on the jubilee line extension." Ph.D. thesis, University of Cambridge, University of Cambridge.

Dimmock, P. S. and Mair, R. J. (2008). "Effect of building stiffness on tunnelling-induced ground movement." *Tunnelling and Underground Space Technology*, 23(4), 438–450.

Farrell, R. P. (2010). "Tunnelling in sands and the response of buildings." Ph.D. thesis, University of Cambridge, University of Cambridge.

Farrell, R. P. and Mair, R. J. (2010). "Centrifuge modelling of the response of buildings to tunnelling." *ICPMG 2010 (Springman, Laue & Seward eds.), Zurich, Switzerland*, 549–554.

Feng, P., Meng, X., Chen, J.-F., and Ye, L. (2015). "Mechanical properties of structures 3D printed with cementitious powders." *Construction and Building Materials*, 93, 486–497.

Franza, A., Marshall, A. M., Haji, T., Abdelatif, A. O., Carbonari, S., and Morici, M. (2017). "A simplified elastic analysis of tunnel-piled structure interaction." *Tunnelling and Underground Space Technology*, 61, 104–121.

Franza, A., Ritter, S., and DeJong, M. J. (2018). "Continuum solutions for tunnel-building interaction and a modified framework for deformation prediction." *Géotechnique*, 0(0), 1–49.

Franzius, J. N., Potts, D. M., and Burland, J. B. (2006). "The response of surface structures to tunnel construction." *Proc. ICE-Geotechnical Engineering*, 159(1), 3–17.

Frischmann, W. W., Hellings, J. E., Gittoes, G., and Snowden, C. (1994). "Protection of the masion house against damage caused by ground movements due to the docklands light railway extension." *Proc. ICE-Geotechnical Engineering*, 107(2), 65–76.

Giardina, G., DeJong, M. J., Chalmers, B., Ormond, B., and Mair, R. J. (2018). "A comparison of current analytical methods for predicting soil-structure interaction due to tunnelling." *Tunnelling and Underground Space Technology*, 79, 319 – 335.

Giardina, G., Hendriks, M. A. N., and Rots, J. G. (2015). "Sensitivity study on tunnelling induced damage to a masonry façade." *Engineering Structures*, 89, 111–129.

Giardina, G., Van de Graaf, A. V., Hendriks, M. A. N., Rots, J. G., and Marini, A. (2013). "Numerical analysis of a masonry façade subject to tunnelling-induced settlements." *Engineering structures*, 54, 234–247.

Goh, K. H. and Mair, R. J. (2011a). "Building damage assessment for deep excavations in Singapore and the influence of building stiffness." *Geot. Eng. J. SEAGS & AGSSEA*, 42(3), 1–12.

Goh, K. H. and Mair, R. J. (2011b). "The horizontal response of framed buildings on individual footings to excavation-induced movements." *Geotechnical Aspects of Underground Construction in Soft Ground (G.M.B. Viggiani ed.), Rome, Italy*, 895–902.

Goh, K. H. and Mair, R. J. (2011c). "The response of buildings to movements induced by deep excavations." *Geotechnical Aspects of Underground Construction in Soft Ground (G.M.B. Viggiani ed.), Rome, Italy*, 903–910.

Lu, Y. C., Bloodworth, A. G., and Gleig, F. D. (2001). "Behaviour of long structures in response to tunnelling." *Proc. Int. Conf. Response of buildings to excavation-induced ground movements, Imperial College, London, CIRIA SP201*, 367–373.

Mair, R. J. (2013). "Tunnelling and deep excavations: Ground movements and their effects." *Proc. 15th European Conf. on Soil Mechanics and Geotechnical Engineering – Geotechnics of Hard Soils – Weak Rocks (Part 4), A. Anagnostopoulos et al. eds., Athens, Greece*, 39–70.

Mair, R. J. and Taylor, R. N. (1997). "Theme lecture: Bored tunneling in the urban environment." *Proc. 14th Int. Conf. on Soil Mechanics and Foundation Engineering, Hamburg, Germany, 6-12 September*, 2353–2385.

Mair, R. J., Taylor, R. N., and Burland, J. B. (1996). "Prediction of ground movements and assessment of risk of building damage due to bored tunnelling." *Geotechnical Aspects of on Underground Construction in Soft Ground (R.J. Mair & R.N. Taylor eds.), London, UK*, 713–718.

Melis, M. J. and Rodriguez Ortiz, J. M. (2001). "Consideration of the stiffness of buildings in the estimation of subsidence damage by EPB tunnelling in the Madrid Subway." *Proc. Int. Conf. Response of buildings to excavation-induced ground movements, Imperial College, London, CIRIA SP201*, 387–394.

Netzel, H. D. (2009). "Building response due to ground movements." Ph.D. thesis, TU Delft, TU Delft.

Pickhaver, J. A., Burd, H. J., and Houlsby, G. T. (2010). "An equivalent beam method to model masonry buildings in 3d finite element analysis." *Computers & structures*, 88, 1049–1063.

Potts, D. M. and Addenbrooke, T. I. (1997). "A structure's influence on tunnelling-induced ground movements.." *Proc. ICE-Geotechnical Engineering*, 125(2), 109–125.

Ritter, S. (2017). "Experiments in tunnel–soil–structure interaction." Ph.D. thesis, University of Cambridge, University of Cambridge.

Ritter, S., DeJong, M. J., Giardina, G., and Mair, R. J. (2017a). "Influence of building characteristics on tunnelling-induced ground movements." *Géotechnique*, 67(10), 926–937.

Ritter, S., DeJong, M. J., Giardina, G., and Mair, R. J. (2018). "3d printing of masonry structures for centrifuge modelling." *9^{th} International Conference on Physical Modelling in Geotechnics 2018, City University of London, United Kingdom, 17-20 July*, xx–xy.

Ritter, S., Giardina, G., DeJong, M. J., and Mair, R. J. (2017b). "Centrifuge modelling of building response to tunnel excavation." *International Journal of Physical Modelling in Geotechnics*, 18(3), 146–161.

Son, M. and Cording, E. J. (2005). "Estimation of building damage due to excavation-induced ground movements." *Journal of Geotechnical and Geoenvironmental Engineering*, 131(2), 162–177.

Son, M. and Cording, E. J. (2007). "Evaluation of building stiffness for building response analysis to excavation-induced ground movements." *Journal of Geotechnical and Geoenvironmental Engineering*, 133(8), 995–1002.

Standing, J. R. (2001). "Paper on Elizabeth House." *Building response to tunnelling–case studies from the Jubilee Line extension. Vol. 2, CIRIA SP200*, 735–754.

Taylor, R. N. and Grant, R. J. (1998). “Centrifuge modelling of the influence of surface structures on tunnelling induced ground movements.” *Tunnels and Metropolises (A. Negro Jr & A.A. Ferreira eds.), World Tunnel Congress ’98, São Paulo, Brazil*, 261–266.

Taylor, R. N. and Yip, D. L. F. (2001). “Centrifuge modelling of the effect of a structure on tunnel-induced ground movements.” *Proc. Int. Conf. Response of buildings to excavation-induced ground movements, Imperial College, London, CIRIA SP201*, 401–432.

Viggiani, G. M. B. and Standing, J. R. (2001). “The Treasury.” *Building response to tunnelling: case studies from construction of the Jubilee Line Extension, volume 2: case studies, London*, 401–432.

Vu, M. N., Broere, W., and Bosch, J. (2016). “Volume loss in shallow tunnelling.” *Tunnelling and Underground Space Technology*, 59, 77–90.

White, D. J., Take, W. A., and Bolton, M. D. (2003). “Soil deformation measurement using particle image velocimetry (piv) and photogrammetry.” *Géotechnique*, 53(7), 619–631.

Yiu, W. N., Burd, H. J., and Martin, C. M. (2017). “Finite-element modelling for the assessment of tunnel-induced damage to a masonry building.” *Géotechnique*, 67(9), 780–794.

List of Tables

TABLE 1. Details of the test series and the 3D printed material properties including density, ρ, flexural strength, f_t, Young's modulus, E, ultimate strain to failure, ε_{ult}, global axial stiffness of the buildings at prototype scale, EA, global bending stiffness of the buildings at prototype scale, EI, and average neutral axis height, h_{NA}.

Test	Model scale				3D printed material properties				Global building stiffness		Neutral axis
	e (mm)	L (mm)	H (mm)	O (%)	ρ (kg/m^3)	f_t (MPa)	E (MPa)	ε_{ult} (%)	EA (kN/m)	EI (kNm^2/m)	h_{NA} (mm)
A	0	200	90	20	1293	1.362	893.1	0.298	$4.49 \cdot 10^5$	$1.48 \cdot 10^6$	34.6
B	160	200	90	20	1278	1.311	800.6	0.357	$4.03 \cdot 10^5$	$1.32 \cdot 10^6$	34.6
C	100	200	90	20	1261	1.130	727.4	0.282	$3.66 \cdot 10^5$	$1.20 \cdot 10^6$	34.6
D	160	200	90	40	1272	0.934	516.0	0.352	$2.04 \cdot 10^5$	$4.05 \cdot 10^5$	29.9
E	130	260	90	20	1280	1.139	689.9	0.309	$3.45 \cdot 10^5$	$1.14 \cdot 10^6$	34.5
F	130	260	90	40	1247	1.702	1039.2	0.246	$4.06 \cdot 10^5$	$8.10 \cdot 10^5$	29.7
Masonry*					1900	0.1-0.9	1000-9000	0.038-0.06†			
Field data‡									$6 \cdot 10^5$-$9 \cdot 10^7$	$7 \cdot 10^3$-$7 \cdot 10^9$	

*The masonry properties are according to Giardina et al. (2015).
†Tensile strain values at the onset of visible cracking for brick walls as observed by Burland and Wroth (1974).
‡Reported by Mair and Taylor (1997) and Dimmock (2003).

TABLE 2. Visible cracking. Tunnel volume loss values refer to crack onset.

Test	$V_{l,t}$ (%)
A	no cracks
B	14.0
C	8.0
D	10.4
E	5.5
F	2.6

List of Figures

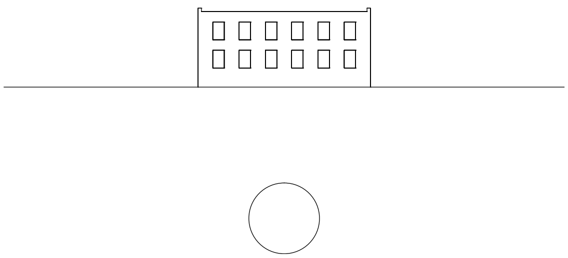

(a) Test A: e/L=0, L/H=2.2, O=20%.

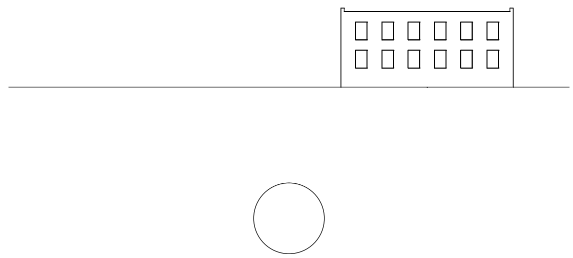

(b) Test B: e/L=0.8, L/H=2.2, O=20%.

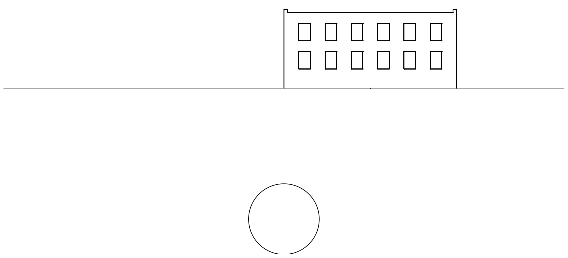

(c) Test C: e/L=0.5, L/H=2.2, O=20%.

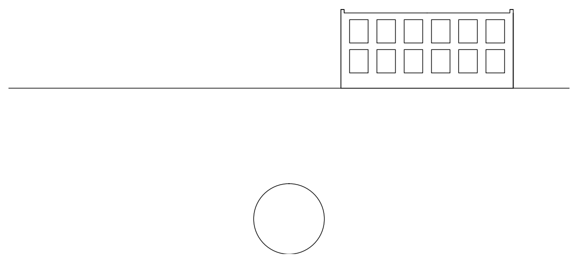

(d) Test D: e/L=0.8, L/H=2.2, O=40%.

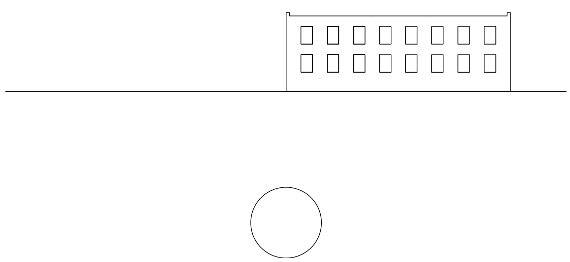

(e) Test E: e/L=0.5, L/H=2.9, O=20%.

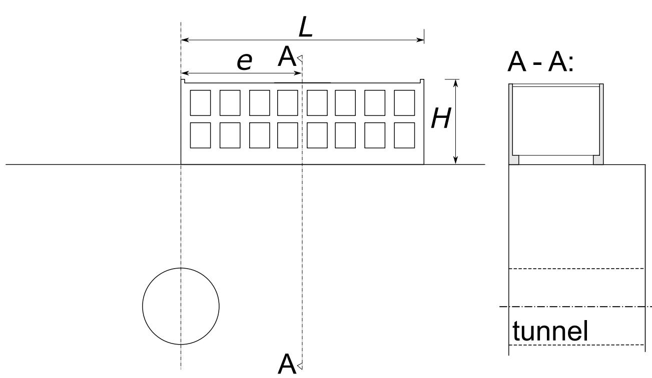

(f) Test F: e/L=0.5, L/H=2.9, O=40%.

Fig. 1. Centrifuge test series with varying building length, L, building eccentricity, e, and façade openings, O.

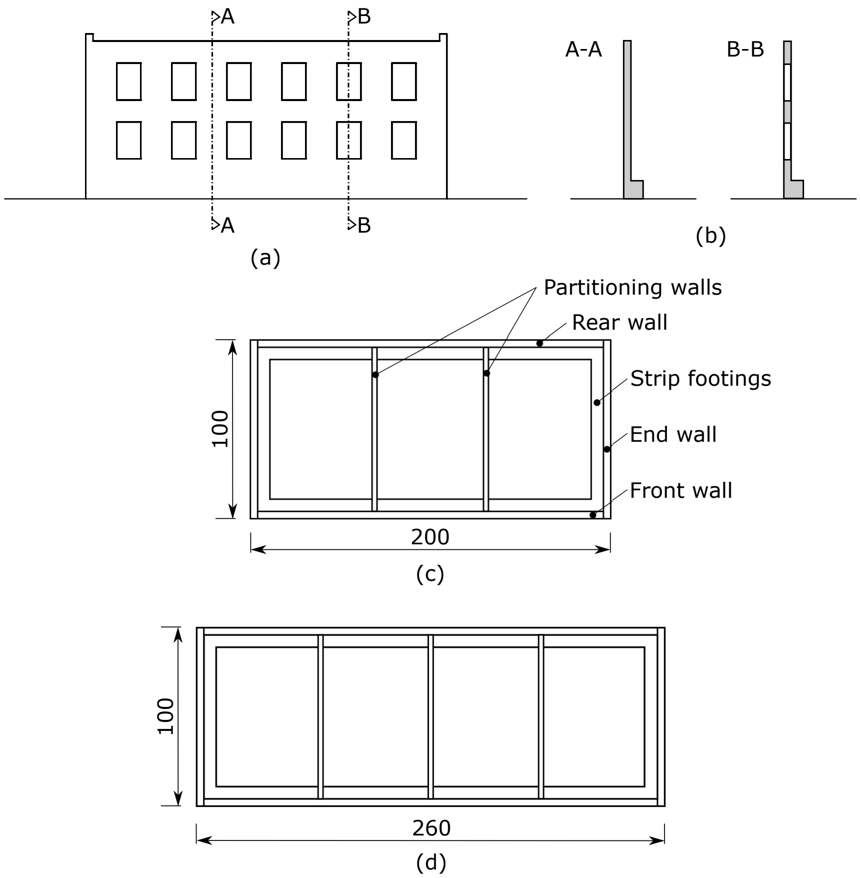

Fig. 2. Building configuration: (a) front view of 200 mm long building, (b) cross-sections of the front façade only (see Fig. 1f), (c) plan view of 200 mm long building and (d) plan view of 260 mm long building. Dimensions in mm.

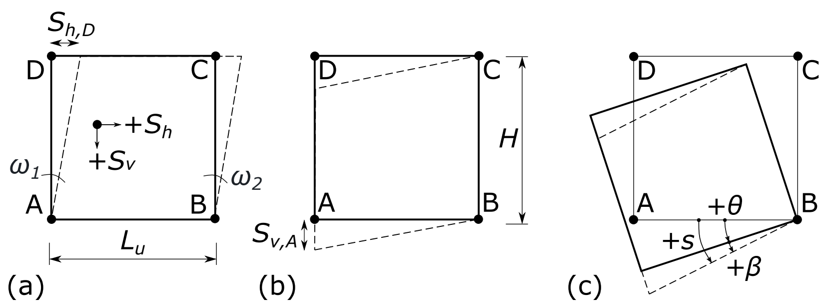

Fig. 3. Building deformation parameters.

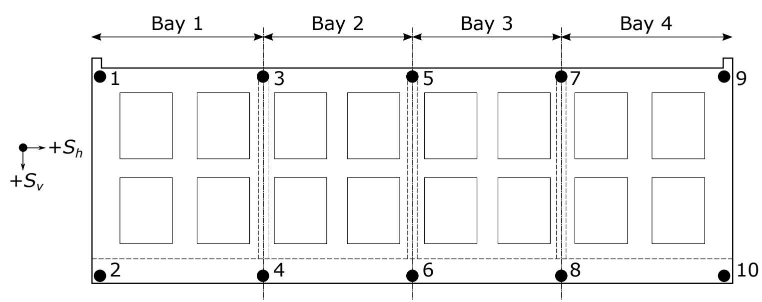

Fig. 4. Subdivision of building at partition walls (dashed vertical lines) into building bays and notation of corner points for a building of 260 mm length.

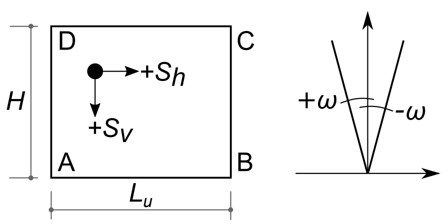

(a) Reference condition for a building unit and sign convention.

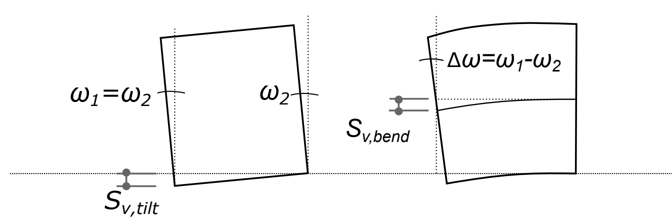

(b) Tilt and bending deformations.

Fig. 5. Framework to investigate building response after Cook (1994).

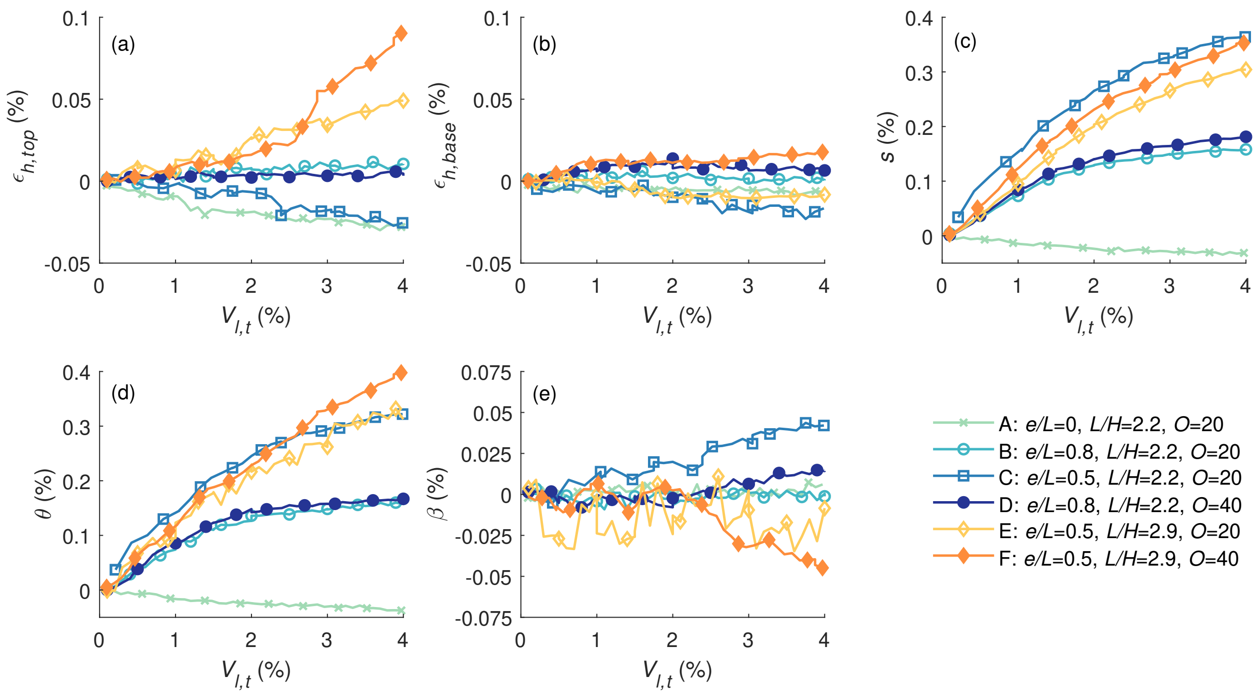

Fig. 6. Global building deformation parameters (no subdivision into bays): (a) top horizontal strain, (b) base horizontal strain, (c) slope, (d) tilt and (e) angular distortion. Positive strains indicate tension.

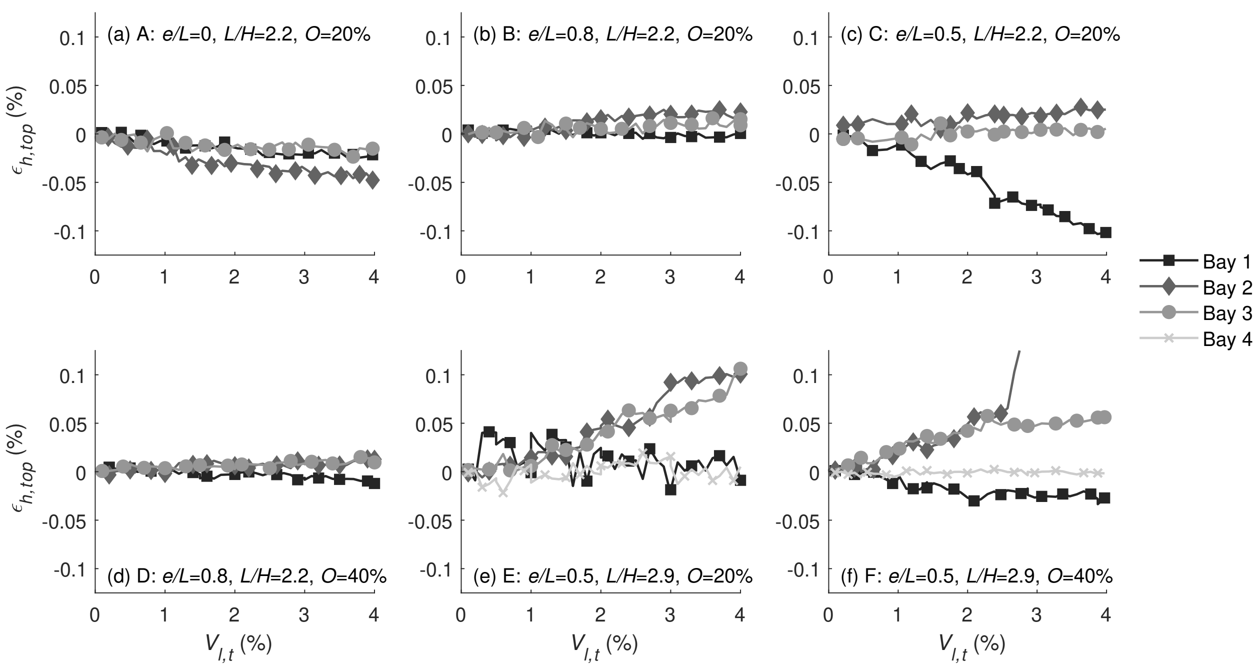

Fig. 7. Top horizontal strain for building bays. Positive strains indicate tension.

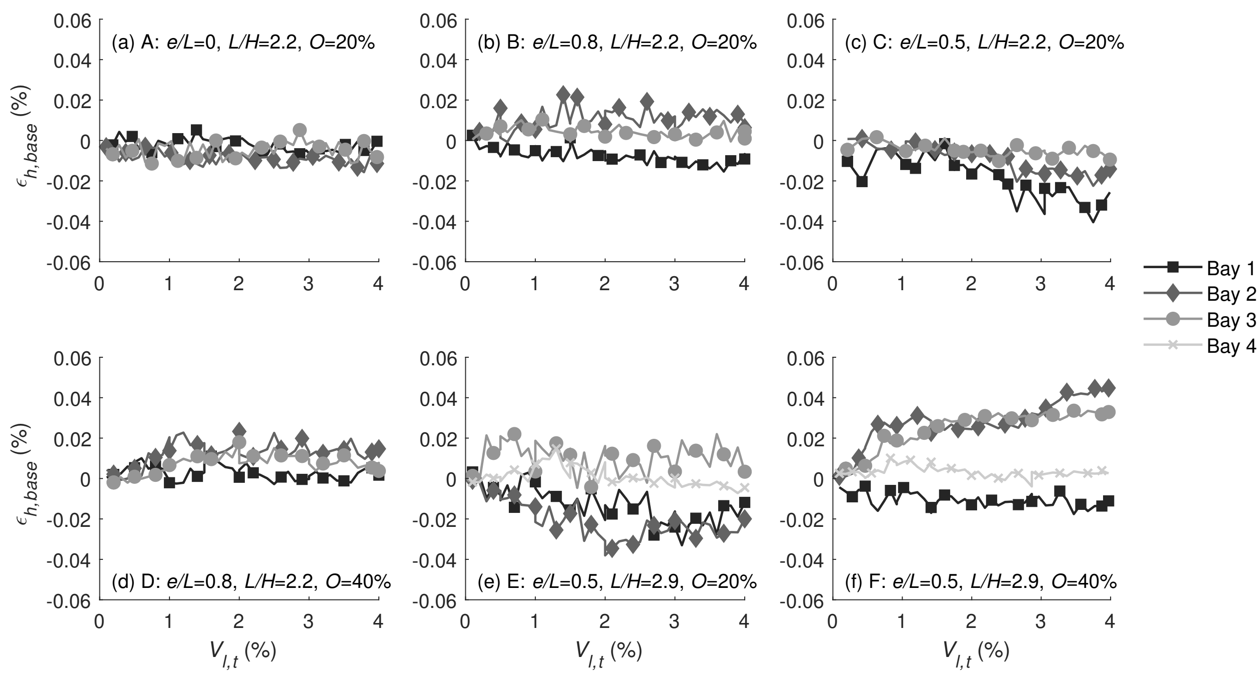

Fig. 8. Base horizontal strain for building bays. Positive strains indicate tension.

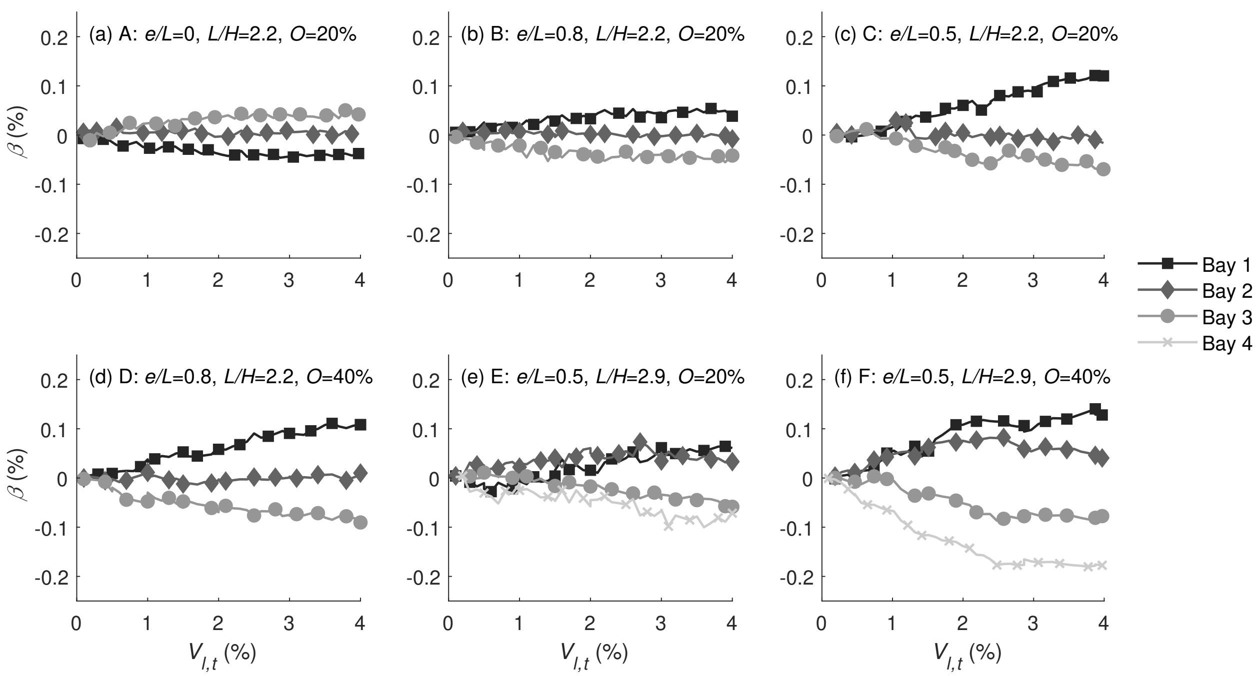

Fig. 9. Angular distortion for building bays.

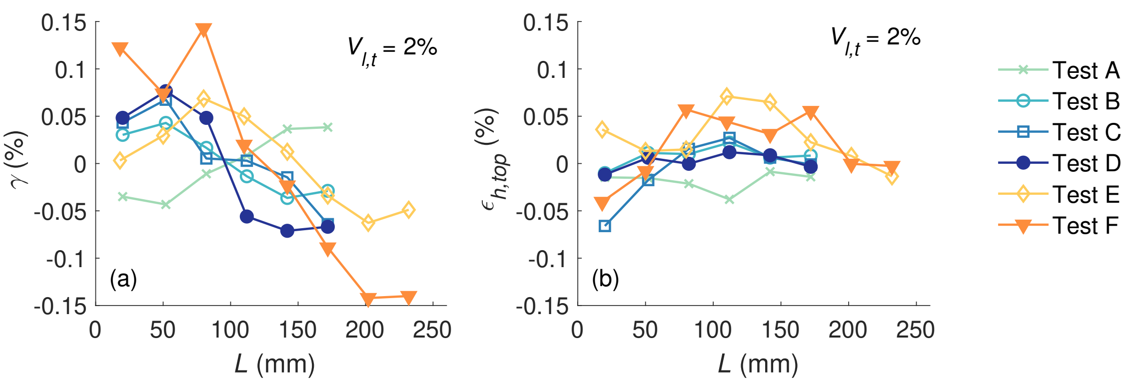

Fig. 10. Distribution of (a) shear strains and (b) top horizontal strain along the building length at $V_{l,t}$ = 2.0%.

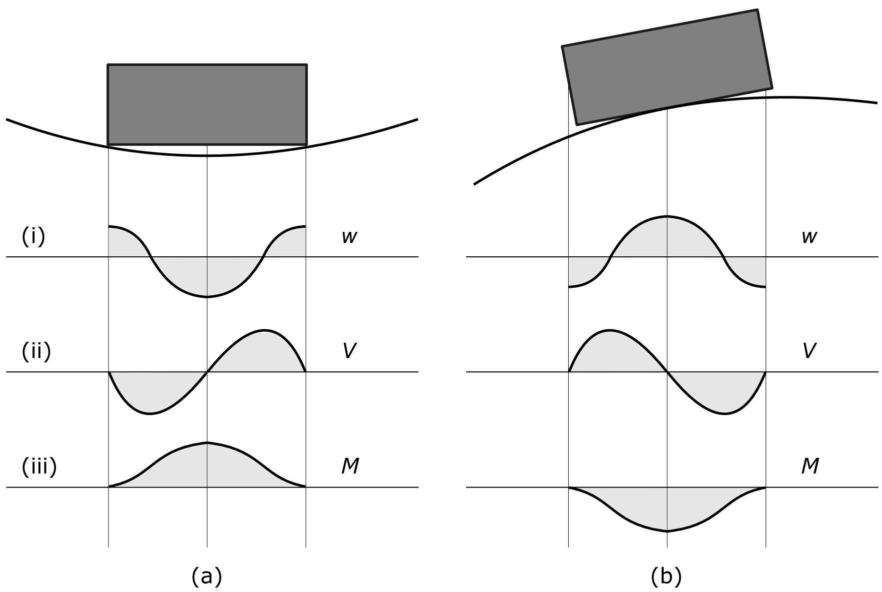

Fig. 11. Mechanical interpretation: (a) sagging and (b) hogging.

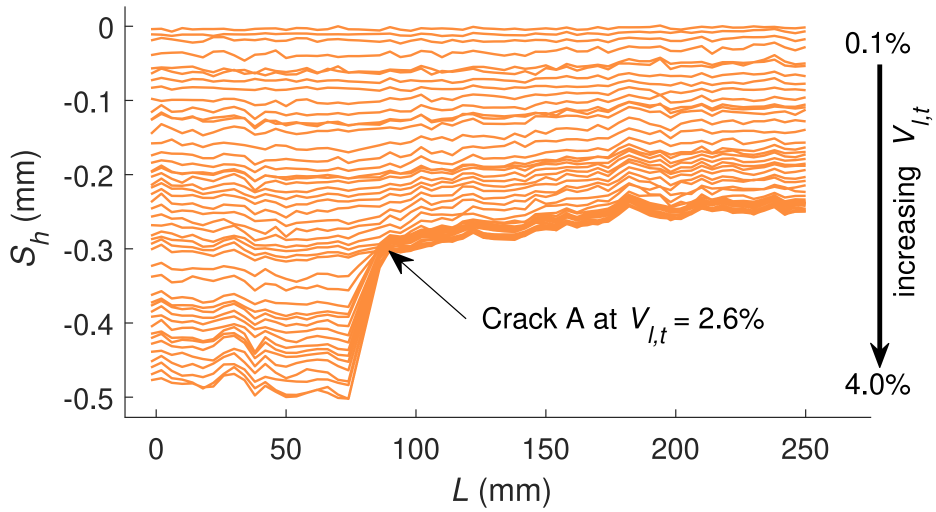

(a) Crack identification using horizontal displacement profiles at top of structure.

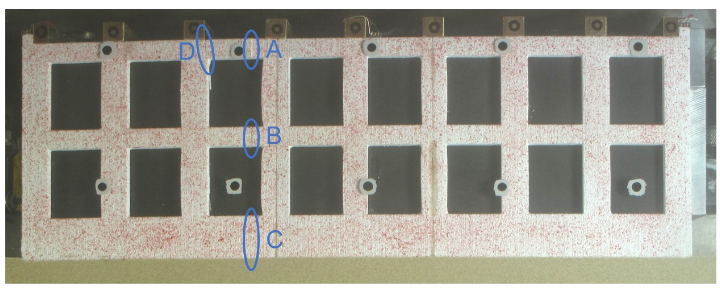

(b) Cracking pattern ($V_{l,t}$ = 6.0%).

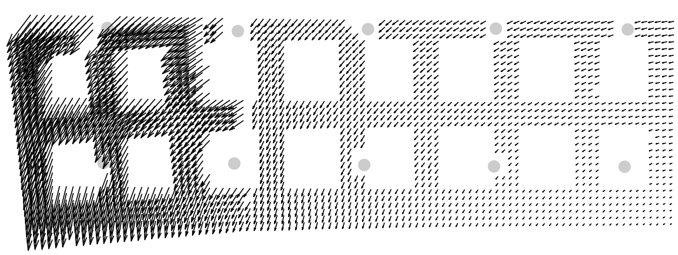

(c) Vector plot at $V_{l,t}$ = 6.0%. Displacement vectors are times 10. Positions of GeoPIV calibration markers are depicted.

Fig. 12. Cracking of test F.

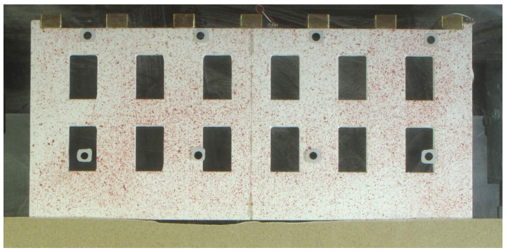

(a) Test A.

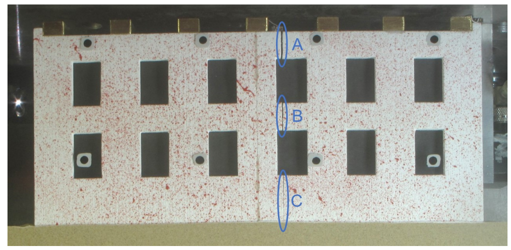

(b) Test B.

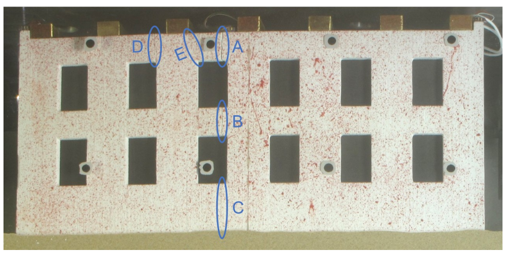

(c) Test C.

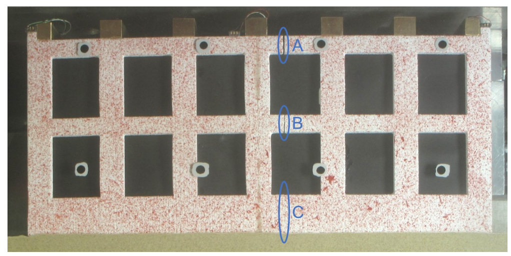

(d) Test D.

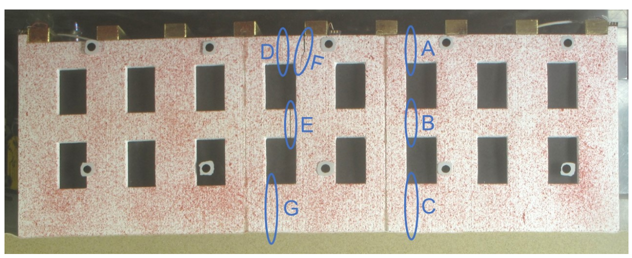

(e) Test E.

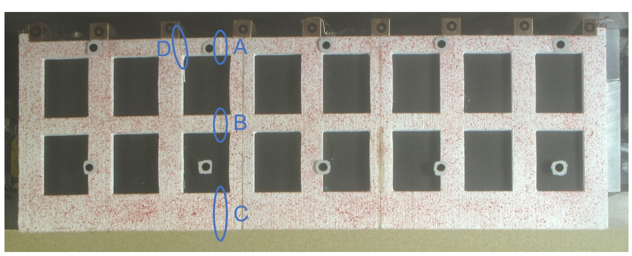

(f) Test F.

Fig. 13. Crack initiation and location. Solid (blue) ovals indicate cracks while dashed (red) ovals show potential micro-cracking. Letters indicate order of crack propagation.

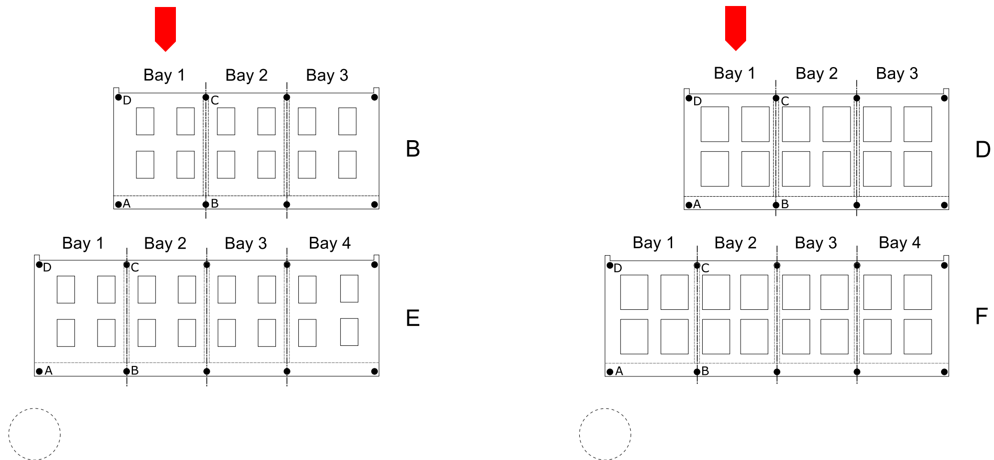

(a) Buildings with 20% openings. **(b)** Buildings with 40% openings.

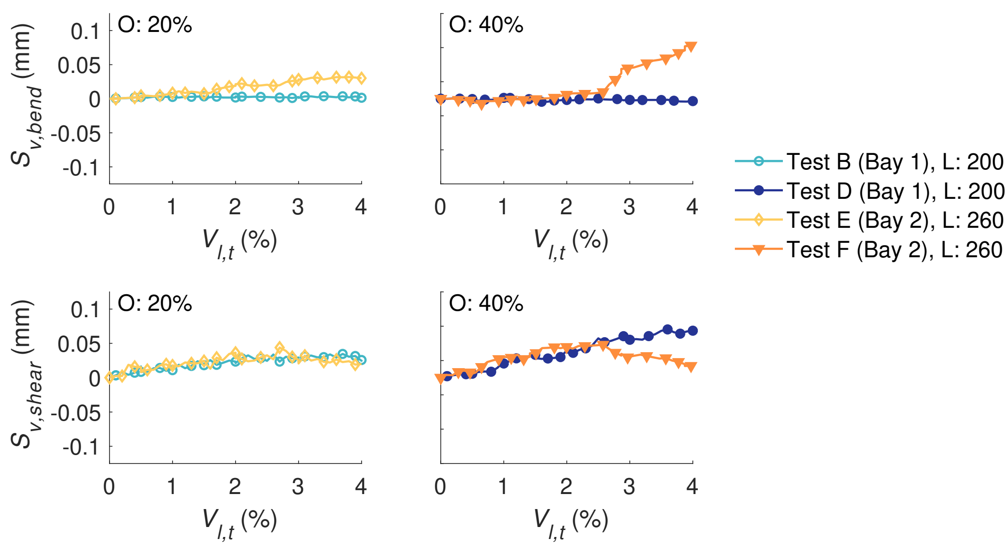

(c) Experimental results.

Fig. 14. Influence of increasing L/H on bending and shear. Tunnel position and diameter in scenarios (a) and (b) are not to scale. The arrows highlight the compared bays.

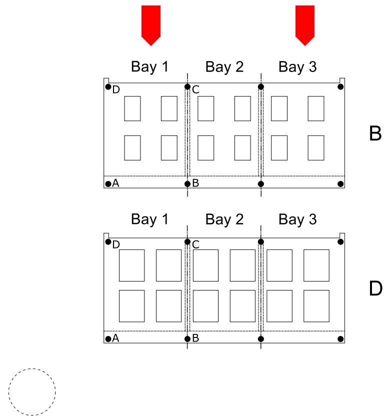

(a) Buildings with L = 200 mm.

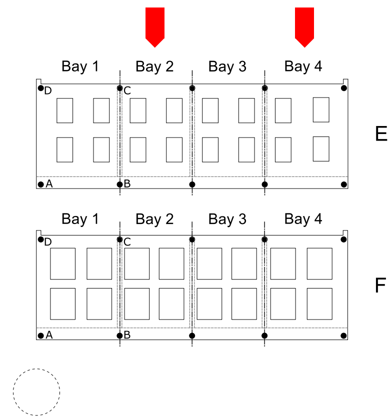

(b) Buildings with L = 260 mm.

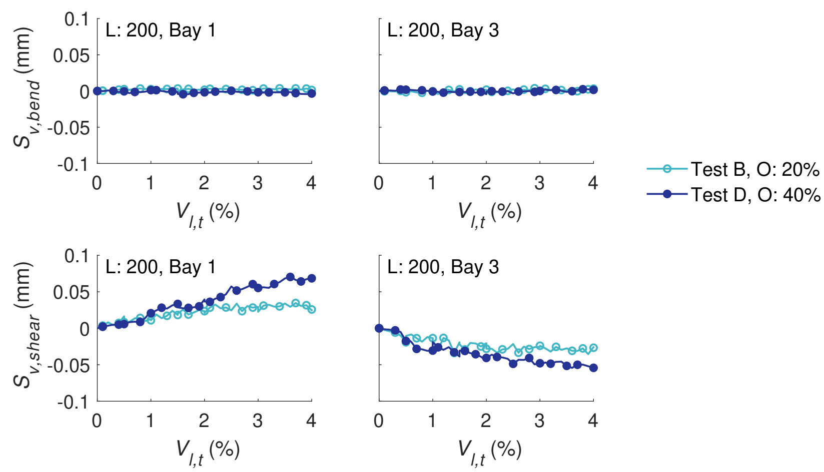

(c) Experimental results for buildings with L = 200 mm.

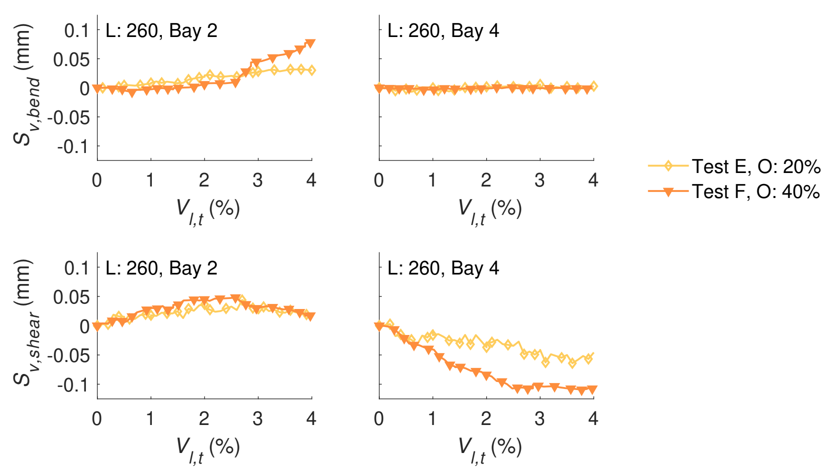

(d) Experimental results for buildings with L = 260 mm.

Fig. 15. Influence of increasing the opening percentage on bending and shear. Tunnel position and diameters in scenarios (a) and (b) are not to scale. The arrows highlight the compared bays.

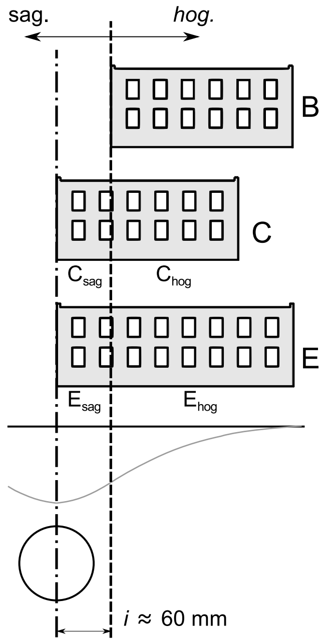

(a) Buildings with O = 20%.

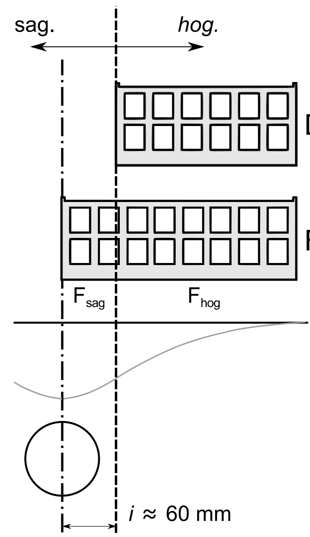

(b) Buildings with O = 40%.

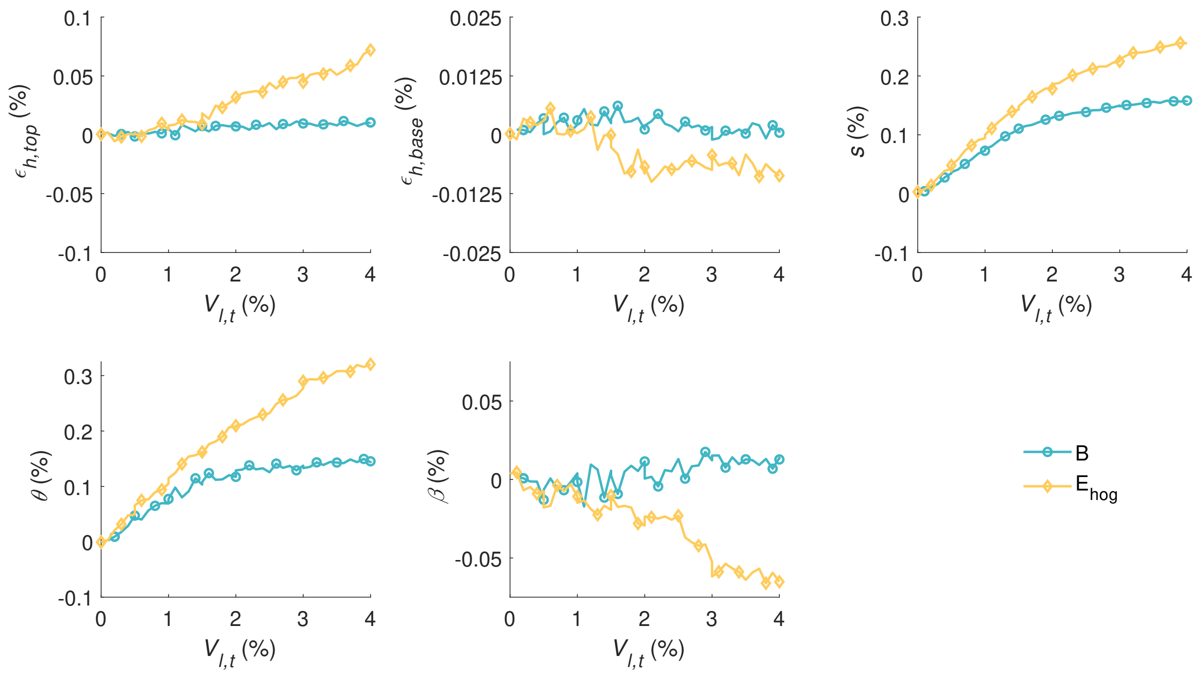

(c) Building deformation parameters for the hogging parts of buildings with 20% façade openings (tensile strains are positive).

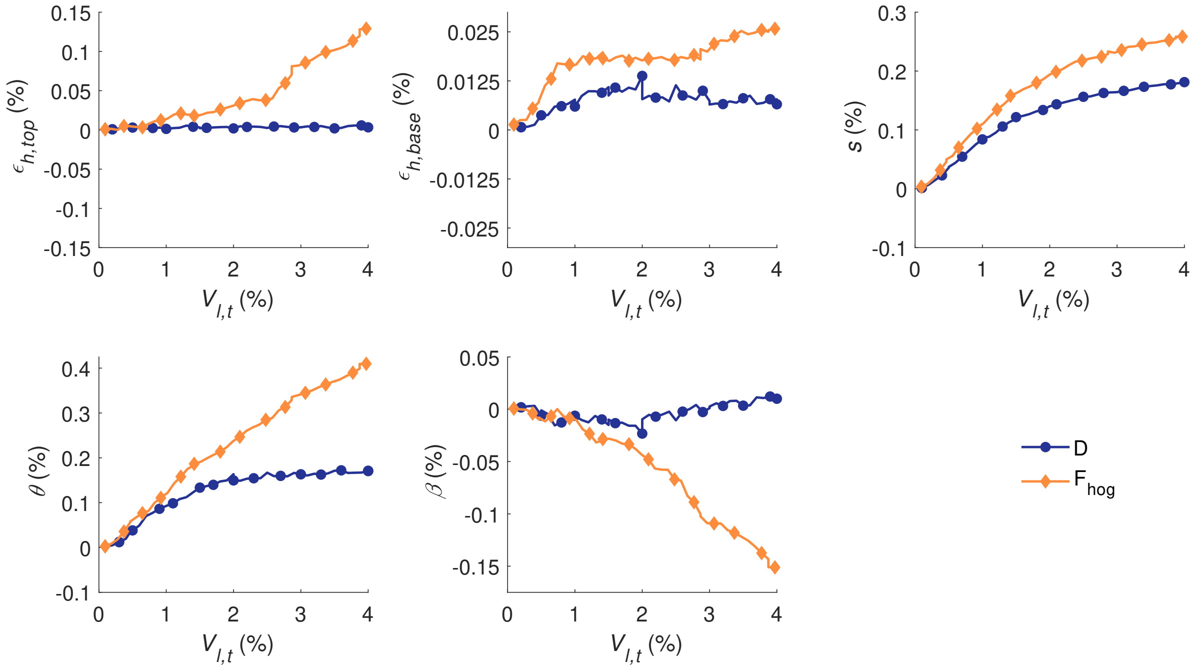

(d) Building deformation parameters for the hogging parts of buildings with 40% façade openings (tensile strains are positive).

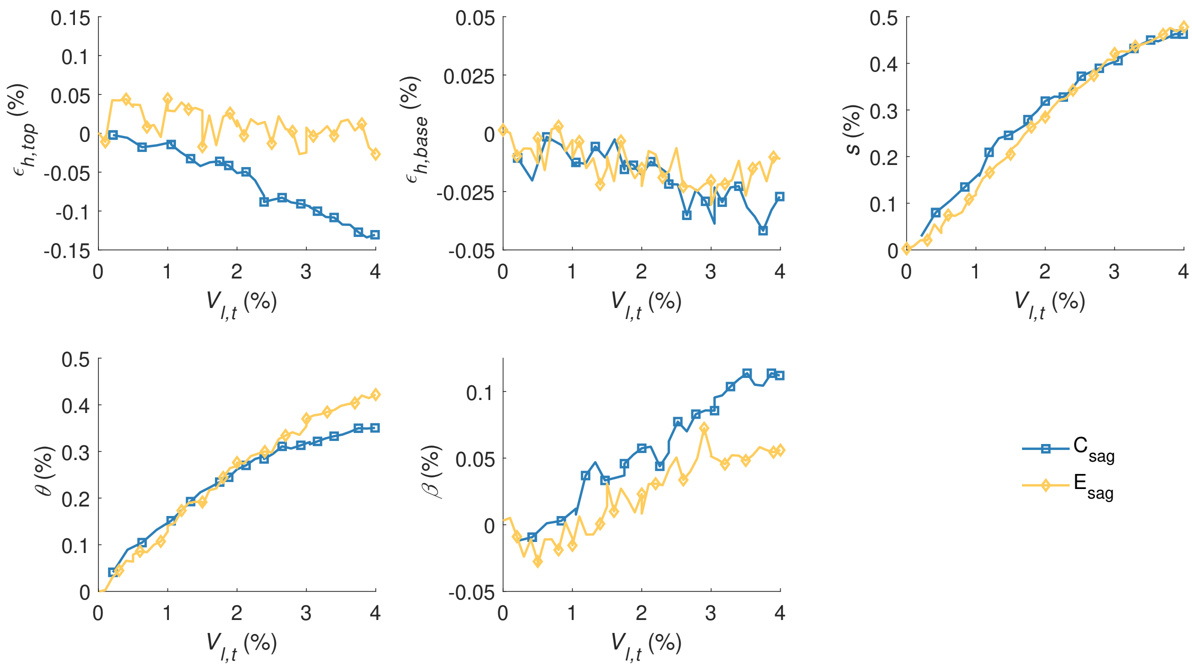

(e) Building deformation parameters for the sagging parts (tensile strains are positive).

Fig. 16. Hogging and sagging separation. (a), (b) scenarios; experimental results: (c), (d), (e).